16. T. Brezesinski, J. Wang, S. H. Tolbert, B. Dunn, *Nat. Mater.* **9**, 146–151 (2010).
17. K. Brezesinski *et al.*, *J. Am. Chem. Soc.* **132**, 6982–6990 (2010).
18. X. Lang, A. Hirata, T. Fujita, M. Chen, *Nat. Nanotechnol.* **6**, 232–236 (2011).
19. V. Augustyn *et al.*, *Nat. Mater.* **12**, 518–522 (2013).
20. S. Ardizzone, G. Fregonara, S. Trasatti, *Electrochim. Acta* **35**, 263–267 (1990).
21. Y. Surendranath, M. W. Kanan, D. G. Nocera, *J. Am. Chem. Soc.* **132**, 16501–16509 (2010).
22. G. A. Snook, P. Kao, A. S. Best, *J. Power Sources* **196**, 1–12 (2011).
23. M. D. Stoller, R. S. Ruoff, *Energy Environ. Sci.* **3**, 1294–1301 (2010).
24. V. Khomenko, E. Frackowiak, F. Béguin, *Electrochim. Acta* **50**, 2499–2506 (2005).
25. Q. Gao, L. Demarconnay, E. Raymundo-Piñero, F. Béguin, *Energy Environ. Sci.* **5**, 9611–9617 (2012).
26. A. F. Burke, Advanced batteries for vehicle applications. In *Encyclopedia of Automotive Engineering*, D. Crolla, D. E. Foster, T. Kobayashi, N. Vaughan, Eds. (Wiley, New York, 2014), pp. 1–20.
27. A. Burke, M. Miller, *J. Power Sources* **196**, 514–522 (2011).
28. D. Linden, T. B. Reddy, *Handbook of Batteries* (McGraw-Hill, New York, ed. 3, 2001).

ACKNOWLEDGMENTS

Supported by National Natural Science Foundation of China grants 51125006, 91122034, 61376056, and 51402336 and Science and Technology Commission of Shanghai grant 14YF1406500. I.W.C. was supported by U.S. Department of Energy BES grant DE-FG02-11ER46814 and used the facilities (Laboratory for Research on the Structure of Matter) supported by NSF grant DMR-11-20901.

SUPPLEMENTARY MATERIALS

www.sciencemag.org/content/350/6267/1508/suppl/DC1
Materials and Methods
Figs. S1 to S14
Tables S1 and S2
References (*29*–*32*)

20 April 2015; accepted 13 November 2015
10.1126/science.aab3798

NANOMATERIALS

Synthesis of borophenes: Anisotropic, two-dimensional boron polymorphs

Andrew J. Mannix,[1,2] Xiang-Feng Zhou,[3,4] Brian Kiraly,[1,2] Joshua D. Wood,[2] Diego Alducin,[5] Benjamin D. Myers,[2,6] Xiaolong Liu,[7] Brandon L. Fisher,[1] Ulises Santiago,[5] Jeffrey R. Guest,[1] Miguel Jose Yacaman,[5] Arturo Ponce,[5] Artem R. Oganov,[8,9,3]* Mark C. Hersam,[2,7,10]* Nathan P. Guisinger[1]*

At the atomic-cluster scale, pure boron is markedly similar to carbon, forming simple planar molecules and cage-like fullerenes. Theoretical studies predict that two-dimensional (2D) boron sheets will adopt an atomic configuration similar to that of boron atomic clusters. We synthesized atomically thin, crystalline 2D boron sheets (i.e., borophene) on silver surfaces under ultrahigh-vacuum conditions. Atomic-scale characterization, supported by theoretical calculations, revealed structures reminiscent of fused boron clusters with multiple scales of anisotropic, out-of-plane buckling. Unlike bulk boron allotropes, borophene shows metallic characteristics that are consistent with predictions of a highly anisotropic, 2D metal.

Bonding between boron atoms is more complex than in carbon; for example, both two- and three-center B-B bonds can form (*1*). The interaction between these bonding configurations results in as many as 16 bulk allotropes of boron (*1*–*3*), composed of icosahedral B_{12} units, small interstitial clusters, and fused supericosahedra. In contrast, small ($n < 15$) boron clusters form simple covalent, quasiplanar molecules with carbon-like aromatic or anti-aromatic electronic structure (*4*–*7*). Recently, Zhai *et al.* have shown that B_{40} clusters form a cage-like fullerene (*6*), further extending the parallels between boron and carbon cluster chemistry.

To date, experimental investigations of nanostructured boron allotropes are notably sparse, partly owing to the costly and toxic precursors (e.g., diborane) typically used. However, numerous theoretical studies have examined two-dimensional (2D) boron sheets [i.e., borophene (*7*)]. Although these studies propose various structures, we refer to the general class of 2D boron sheets as borophene. Based upon the quasiplanar B_7 cluster (Fig. 1A), Boustani proposed an Aufbau principle (*8*) to construct nanostructures, including puckered monolayer sheets (analogous to the relation between graphene and the aromatic ring). The stability of these sheets is enhanced by vacancy superstructures (*7*, *9*) or out-of-plane distortions (*10*, *11*). Typically, borophene is predicted to be metallic (*7*, *9*–*12*) or semimetallic (*10*) and is expected to exhibit weak binding (*13*) and anisotropic growth (*14*) when adsorbed on noble-metal substrates. Early reports of multiwall boron nanotubes suggested a layered structure (*15*), but their atomic-scale structure remains unresolved. It is therefore unknown whether borophene is experimentally stable and whether the borophene structure would reflect the simplicity of planar boron clusters or the complexity of bulk boron phases.

We have grown atomically thin, borophene sheets under ultrahigh-vacuum (UHV) conditions (Fig. 1B), using a solid boron atomic source (*99.9999*% purity) to avoid the difficulties posed by toxic precursors. An atomically clean Ag(111) substrate provided a well-defined and inert surface for borophene growth (*13*, *16*). In situ scanning tunneling microscopy (STM) images show the emergence of planar structures exhibiting anisotropic corrugation, which is consistent with first-principles structure prediction. We further verify the planar, chemically distinct, and atomically thin nature of these sheets via a suite of characterization techniques. In situ electronic characterization supports theoretical predictions that borophene sheets are metallic with highly anisotropic electronic properties. This anisotropy is predicted to result in mechanical stiffness comparable to that of graphene along one axis. Such properties are complementary to those of existing 2D materials and distinct from those of the metallic boron previously observable only at ultrahigh pressures (*17*).

During growth, the substrate was maintained between 450° and 700°C under a boron flux between ~0.01 to ~0.1 monolayer (ML) per minute [see supplementary materials for details (*18*)]. After deposition, in situ Auger electron spectroscopy (AES; Fig. 1C) revealed a boron KLL peak at the standard position (180 eV) superimposed on the clean Ag(111) spectrum. We observed no peaks due to contaminants, and none of the distinctive peak shifts or satellite features characteristic of compound or alloy formation (fig. S1).

After boron deposition at a substrate temperature of 550°C, STM topography images (Fig. 1D) revealed two distinct boron phases: a homogeneous phase and a more corrugated "striped" phase (highlighted with red and white arrows, respectively). Simultaneously acquired dI/dV maps (where I and V are the tunneling current and voltage, respectively) of the electronic density of states (DOS), given in Fig. 1E, showed strong electronic contrast between boron sheets and the Ag(111) substrate and increased differentiation between homogeneous and striped islands. The relative concentration of these phases depends upon the deposition rate. Low deposition rates favored the striped phase and resulted in the

[1]Center for Nanoscale Materials, Argonne National Laboratory, 9700 South Cass Avenue, Building 440, Argonne, IL 60439, USA. [2]Department of Materials Science and Engineering, Northwestern University, 2220 Campus Drive, Evanston, IL 60208, USA. [3]Department of Geosciences, Center for Materials by Design, and Institute for Advanced Computational Science, Stony Brook University, Stony Brook, NY 11794, USA. [4]School of Physics, Nankai University, Tianjin 300071, China. [5]Department of Physics, University of Texas San Antonio, San Antonio, TX 78249, USA. [6]NU*ANCE* Center, Northwestern University, 2220 Campus Drive, Evanston, IL 60208, USA. [7]Applied Physics Graduate Program, Northwestern University, 2220 Campus Drive, Evanston, IL 60208, USA. [8]Skolkovo Institute of Science and Technology, Skolkovo Innovation Center, 5 Nobel Street, Moscow 143026, Russia. [9]Moscow Institute of Physics and Technology, 9 Institutskiy Lane, Dolgoprudny City, Moscow Region, 141700, Russia. [10]Department of Chemistry, Northwestern University, 2220 Campus Drive, Evanston, IL 60208, USA.
***Corresponding author. E-mail: nguisinger@anl.gov (N.P.G.); m-hersam@northwestern.edu (M.C.H.); artem.oganov@stonybrook.edu (A.R.O.)**

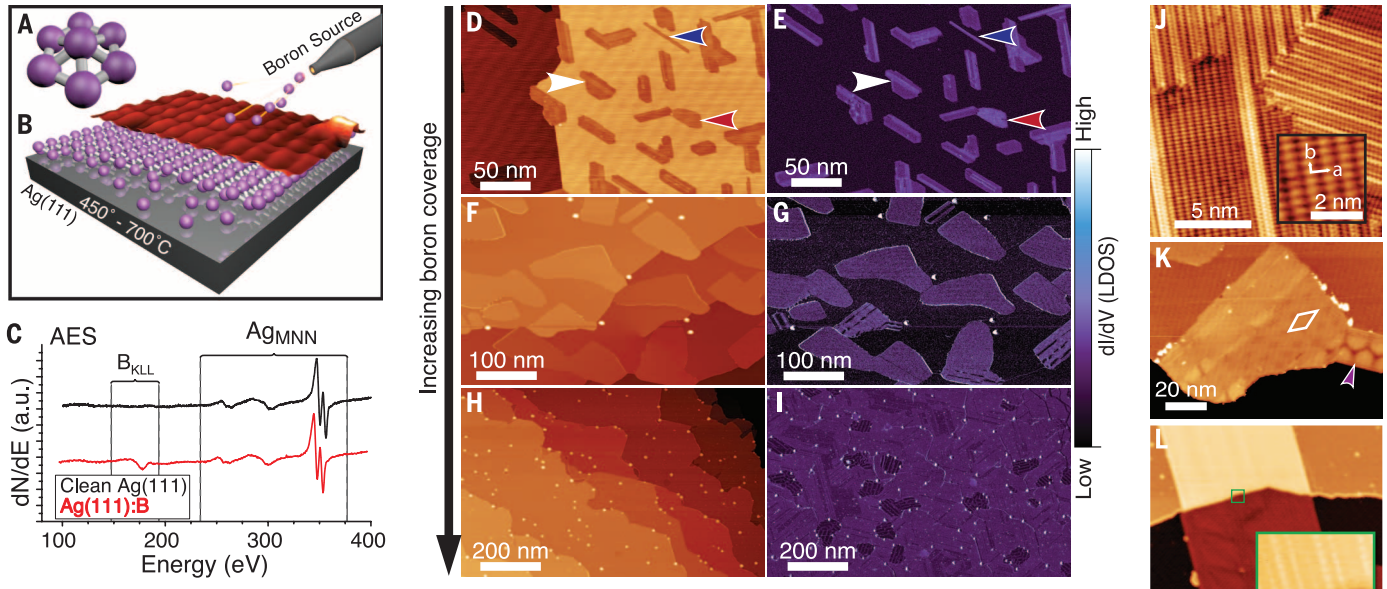

Fig. 1. Growth and atomic-scale characterization of borophene sheets. Schematics of (**A**) distorted B_7 cluster and (**B**) growth setup with atomic structure model and STM topography rendering. (**C**) AES spectra of clean Ag(111) before and after boron deposition. (**D** to **I**) Series of large-scale STM topography (left) and closed-loop *dI/dV* (right) images of borophene sheets, showing (D and E) low coverage (V_{sample} = 2.0 V, I_t = 100 pA), (F and G) medium coverage (V_{sample} = 3.5 V, I_t = 100 pA), and (H and I) high coverage (V_{sample} = 3.5 V, I_t = 100 pA). Regions of homogeneous-phase, striped-phase island, and striped-phase nanoribbon are indicated with red, white, and blue arrows, respectively. (**J** to **L**) STM topography images showing (J) striped-phase atomic-scale structure (V_{sample} = 0.1 V, I_t = 1.0 nA). Inset shows rectangular lattice with overlaid lattice vectors. (K) Striped phase with rhombohedral (indicated by white rhombus) and honeycomb (indicated by purple arrow) Moiré patterns (V_{sample} = 3.5 V, I_t = 100 pA). (L) Striped-phase island, demonstrating carpet-mode growth (V_{sample} = 3.5 V, I_t = 100 pA). Inset shows atomic continuity across the Ag(111) step (V_{sample} = −0.5 V, I_t = 700 pA).

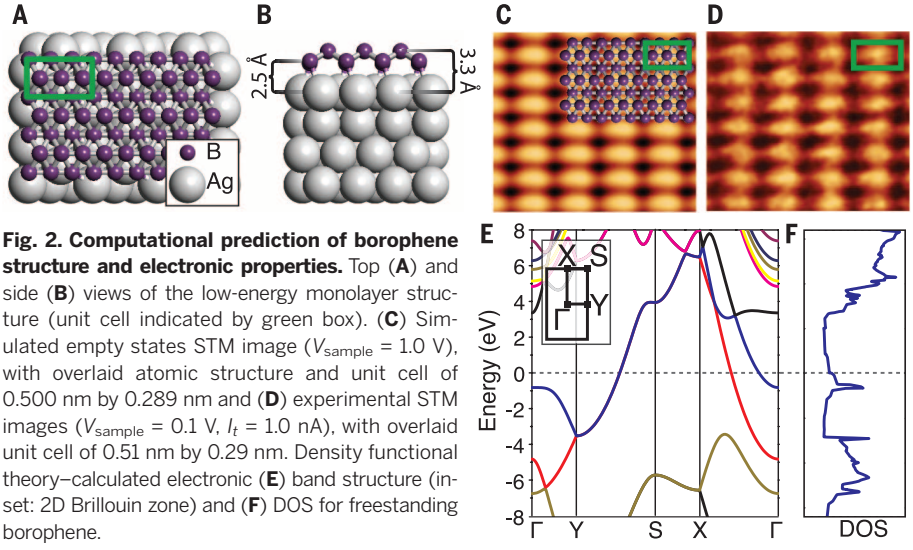

Fig. 2. Computational prediction of borophene structure and electronic properties. Top (**A**) and side (**B**) views of the low-energy monolayer structure (unit cell indicated by green box). (**C**) Simulated empty states STM image (V_{sample} = 1.0 V), with overlaid atomic structure and unit cell of 0.500 nm by 0.289 nm and (**D**) experimental STM images (V_{sample} = 0.1 V, I_t = 1.0 nA), with overlaid unit cell of 0.51 nm by 0.29 nm. Density functional theory–calculated electronic (**E**) band structure (inset: 2D Brillouin zone) and (**F**) DOS for freestanding borophene.

growth of striped-phase nanoribbons (blue arrow, also fig. S2). At higher deposition rates, we observed more of the homogeneous islands (Fig. 1, F and G). Increasing growth temperatures favored the striped phase, suggesting that the homogeneous phase is metastable relative to the striped phase. Both phases exhibited threefold orientation degeneracy with respect to the substrate, as confirmed by low-energy electron diffraction (fig. S3). The island size for both phases resembles that of graphene grown on Ag(111) (*19*).

At boron coverage approaching 1.0 ML, the substrate is completely covered by boron sheets and sparse clusters (Fig. 1, H and I).

High-resolution STM images show anisotropic atomic-scale features for both phases. The homogeneous phase (fig. S4) appears as atomic chains (0.30 nm periodicity) with periodic vertical buckling, a short-range rhombohedral Moiré pattern, and a longer-range 1D Moiré pattern (fig. S4). The striped phase (Fig. 1J) consists of a rectangular lattice commensurate with regions of striped corrugation. The rectangular structure (inset) is defined by vectors **a** and **b** of lengths 0.51 nm (±0.02 nm) and 0.29 nm (±0.02 nm), respectively. Within the striped regions, the in-plane periodicity parallel to the **a** vector is reduced by the increased out-of-plane corrugation associated with the stripes. However, the periodicities along the stripes match those of the rectangular lattice in the **b** direction. Further analysis [see supplementary text (*18*)] shows that the striped regions are simple distortions of the rectangular lattice that maximize the number of ideal boron adsorption sites (fig. S5). The formation of these stripes was temperature-dependent, with fewer stripes observed at 450°C and almost complete stripe coverage at 700°C. This is consistent with a progressive, thermally driven relaxation of the rectangular lattice into more favorable adsorption sites.

Rotationally misaligned striped-phase islands coalesce via defects that accommodate the anisotropic corrugations to form a complete monolayer (fig. S5). As shown in Fig. 1K, the striped regions exhibited Moiré patterns with rhombohedral (~8 nm period, marked by white rhombus) or, far less commonly, honeycomb (indicated by purple arrow) symmetry. These observations indicate the possibility of at least two well-defined long-range structural relationships between borophene and Ag(111). The borophene superstructure is evidently more complex than planar 2D materials such as BN, which forms a well-defined nanomesh on transition metals (*20*, *21*) due to substrate interactions. The mildly attractive B-Ag

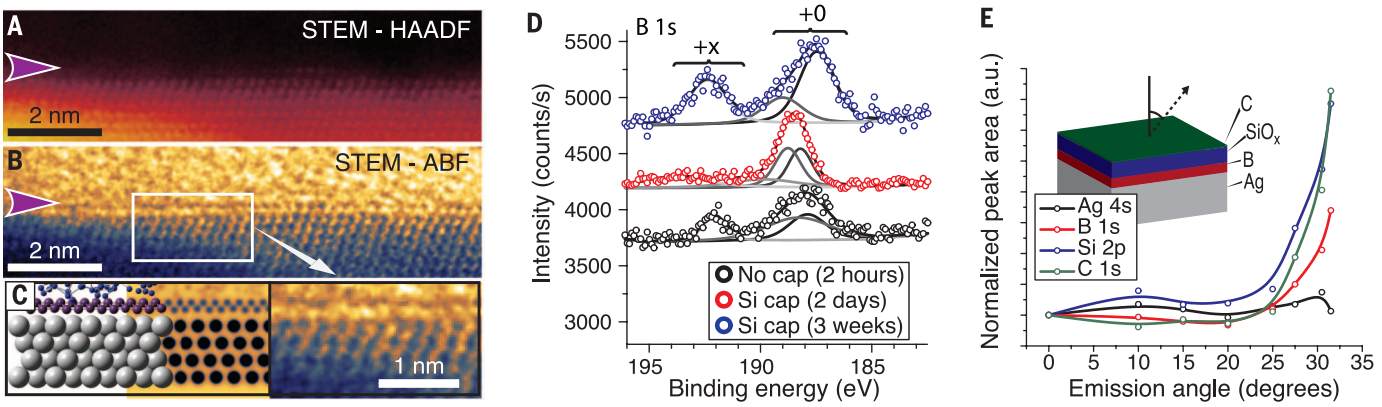

Fig. 3. Borophene structural and chemical characterization. Cross-sectional AC-STEM images from (**A**) HAADF and (**B**) ABF detectors. (C) Juxtaposition (left to right) of Si-capped borophene structure model, simulated ABF image, and magnified ABF image. (**D**) XPS B 1s core–level spectra and fitted components for samples with and without Si capping layers. (**E**) Angle-resolved XPS data acquired on Si-capped samples. Inset: schematic showing measurement angle and sample structure determined by angle-resolved XPS.

interactions, (*21*) result in enhanced corrugation and substrate-stabilized structural variation in borophene, providing additional degrees of freedom for functionality beyond those of conventional 2D materials.

Frequently, borophene growth over the substrate step edges is observed [i.e., "carpet mode" growth (*22*)], as in Fig. 1L. This continuity of the atomic-scale structure over the step (inset) suggests that the borophene is structurally distinct from the underlying substrate.

These experimental results are further elucidated by ab initio evolutionary structure prediction with the USPEX algorithm (*23*, *24*), which minimizes the thermodynamic potential of the system using density functional theory (DFT). Structures calculated with varying concentrations of Ag and B atoms on the Ag(111) substrate show surface segregation of B (fig. S6), indicating that the formation of a B-Ag surface alloy or boride is highly improbable (*16*, *25*). Additional calculations predict likely monolayer (fig. S7) and bilayer (fig. S8) borophene structures on Ag(111), although height measurements (see following discussion) supported a monolayer model.

The lowest-energy monolayer structure is shown in Fig. 2, A and B, and is constructible from distorted B_7 clusters using the Aufbau principle proposed by Boustani (*8*). The symmetry (space group *Pmmn*) and calculated lattice constants agree well with the STM data, with **a** and **b** equal to 0.500 nm and 0.289 nm, respectively. Comparison between simulated (Fig. 2C) and experimental STM topography images (Fig. 2D, also fig. S7) gives excellent agreement, as do electron diffraction data (fig. S3). Freestanding relaxation of this structure removes the slight corrugations along the **a** direction, but preserves the buckling along the **b** direction (fig. S7). The freestanding sheet may exhibit instability against long-wavelength transversal thermal vibrations (fig. S7), which may contribute to the observed stripe formation and would likely distort the structure of the borophene sheet upon removal from the growth substrate. This substrate-induced stability frames borophene as an intermediate class of templated, covalently bound sheets with properties distinct from those of conventional 2D materials and more consistent structure than that of supported silicon phases (*26*).

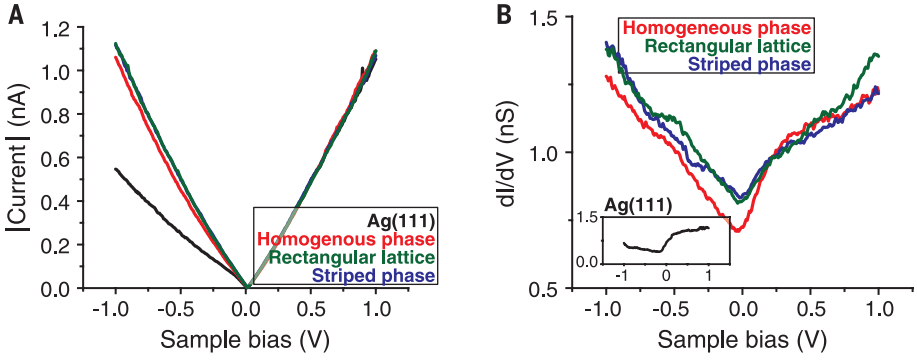

Fig. 4. Scanning tunneling spectroscopy of borophene. (**A**) STS *I-V* curves and (**B**) STS *dI/dV* spectra [inset: clean Ag(111) dI/dV spectrum] from the borophene sheets, which demonstrate metallic characteristics (feedback loop opened at V_{sample} = 1.0 V, I_t = 1.0 nA).

Electronic band structure calculations (Fig. 2E) within the 2D Brillouin zone of the relaxed, freestanding monolayer (inset) predict metallic conduction (i.e., bands crossing the Fermi level) along the Γ-*X* and *Y*-*S* directions (parallel to the uncorrugated **a** direction). However, the out-of-plane corrugation along the **b** direction opens a band gap along the Γ-*Y* and *S*-*X* directions. As a result, borophene is a highly anisotropic metal, where electrical conductivity is confined along the chains. The calculated DOS (Fig. 2F) is likewise metallic (*9*, *11*).

This structure also results in substantial mechanical anisotropy (fig. S7). Owing to the strong, highly coordinated B-B bonds, the in-plane Young's modulus (a measure of stiffness) is equal to 170 GPa·nm along the **b** direction, and 398 GPa·nm along the **a** direction, which potentially rivals graphene, at 340 GPa·nm (*27*). Furthermore, the out-of-plane buckling results in negative values for the in-plane Poisson's ratio (equal to –0.04 along **a** and –0.02 along **b**), resulting in unusual properties, such as in-plane expansion under tensile strain.

The apparent topographic height of the boron islands in STM depended upon scanning parameters, with the islands appearing as depressions for sample biases <3.2 V (compare the images in Fig. 1, D and F). This observation is attributed to the inherent convolution between topography and electronic structure in STM measurements. Similar inversion is observed for NaCl islands (*28*) and graphene (*19*) on Ag(111). However, cross-sectional, aberration-corrected scanning transmission electron microscopy (AC-STEM) unambiguously shows that the boron phase is atomically thin and structurally distinct from the Ag(111) growth substrate. AC-STEM sample preparation is detailed in fig. S9. Images acquired with the high-angle annular dark field (HAADF) detector (Fig. 3A) are sensitive to the atomic number *Z* (contrast ~ $Z^{3/2}$) and show minimal contrast at the interface between the Ag(111) substrate and amorphous SiO_x capping layer, which is consistent with the lack of electron scattering from the low-*Z* boron. Nevertheless, electron energy-loss spectra confirm that the boron lies at the Ag(111) surface (fig. S11). Annular bright field (ABF) images (Fig. 3B and fig. S10), which are

sensitive to light elements such as boron (*29*), revealed a planar structure (indicated by a purple arrow) at this interface. The observed contrast and structure are consistent with a simulated ABF image of the borophene structure model (Fig. 3C). Measured sheet thicknesses of ~0.27 to ~0.31 nm match both the monolayer structure model and multiwalled boron nanotubes (*15*).

X-ray photoelectron spectroscopy (XPS) measures both sample composition and the oxidation state of the species present. Although the borophene islands persisted under ambient conditions (fig. S12), the emergence of higher–binding energy features in the XPS B 1s core-level spectra (Fig. 3D) demonstrate that bare samples (black curve) were partially oxidized within several hours in ambient conditions. However, this oxidation was impeded by an amorphous silicon/silicon oxide capping layer (red curve), which delayed oxidation for several weeks (blue curve). The unoxidized, capped sample is fit by two Voigt components, which reflect the differences in chemical environment between the low- and high-buckled atoms. Increasing the photoelectron detector angle from the sample normal enhances XPS surface sensitivity, thereby selectively probing the surface and subsurface. The normalized, integrated components of angle-resolved XPS spectra on silicon-capped borophene are plotted in Fig. 3E. With increasing emission angle, the relative intensities of the carbon, silicon, and boron peaks increased, whereas the silver peak diminished. These results confirm the structure shown in the inset schematic, corroborating our AES, STM, and STEM results. Additional XPS data are given in fig. S13.

As shown above, theoretical predictions of the borophene structure forecast metallic characteristics. However, all known bulk boron allotropes are semiconductors at standard conditions, only becoming metallic at extremely high pressures (*17*). Scanning tunneling spectroscopy (STS) confirms the metallic characteristics of borophene through *I*–*V* curves (Fig. 4A) and *dI*/*dV* spectra (which measure the local electronic DOS, Fig. 4B). These show gapless (i.e., metallic) behavior consistent with the superposition between the Ag(111) surface (*30*) and the predicted filled-state population in borophene (Fig. 2G). These observations are likely to motivate and inform further studies of metallicity and related phenomena in 2D boron polymorphs.

REFERENCES AND NOTES

1. T. Ogitsu, E. Schwegler, G. Galli, *Chem. Rev.* **113**, 3425–3449 (2013).
2. B. Douglas, S.-M. Ho, *Structure and Chemistry of Crystalline Solids* (Springer Science & Business Media, New York, 2007).
3. A. R. Oganov *et al*., *Nature* **457**, 863–867 (2009).
4. H.-J. Zhai, B. Kiran, J. Li, L.-S. Wang, *Nat. Mater.* **2**, 827–833 (2003).
5. A. P. Sergeeva *et al*., *Acc. Chem. Res.* **47**, 1349–1358 (2014).
6. H.-J. Zhai *et al*., *Nat. Chem.* **6**, 727–731 (2014).
7. Z. A. Piazza *et al*., *Nat. Commun.* **5**, 3113 (2014).
8. I. Boustani, *Phys. Rev. B* **55**, 16426–16438 (1997).
9. H. Tang, S. Ismail-Beigi, *Phys. Rev. Lett.* **99**, 115501 (2007).
10. X.-F. Zhou *et al*., *Phys. Rev. Lett.* **112**, 085502 (2014).
11. K. C. Lau, R. Pandey, *J. Phys. Chem. C* **111**, 2906–2912 (2007).
12. E. S. Penev, S. Bhowmick, A. Sadrzadeh, B. I. Yakobson, *Nano Lett.* **12**, 2441–2445 (2012).
13. Y. Liu, E. S. Penev, B. I. Yakobson, *Angew. Chem. Int. Ed.* **52**, 3156–3159 (2013).
14. H. Liu, J. Gao, J. Zhao, *Sci. Rep.* **3**, 3238 (2013).
15. F. Liu *et al*., *J. Mater. Chem.* **20**, 2197 (2010).
16. H. Okamoto, *J. Phase Equilibria* **13**, 211–212 (1992).
17. M. I. Eremets, V. V. Struzhkin, H. Mao, R. J. Hemley, *Science* **293**, 272–274 (2001).
18. Additional supplementary text and data are available on *Science* Online.
19. B. Kiraly *et al*., *Nat. Commun.* **4**, 2804 (2013).
20. S. Berner *et al*., *Angew. Chem.* **46**, 5115–5119 (2007).
21. F. Müller *et al*., *Phys. Rev. B* **82**, 113406 (2010).
22. H. I. Rasool *et al*., *J. Am. Chem. Soc.* **133**, 12536–12543 (2011).
23. A. R. Oganov, C. W. Glass, *J. Chem. Phys.* **124**, 244704–244716 (2006).
24. Q. Zhu, L. Li, A. R. Oganov, P. B. Allen, *Phys. Rev. B* **87**, 195317 (2013).
25. A. Kolmogorov, S. Curtarolo, *Phys. Rev. B* **74**, 224507 (2006).
26. B. Feng *et al*., *Nano Lett.* **12**, 3507–3511 (2012).
27. C. Lee, X. Wei, J. W. Kysar, J. Hone, *Science* **321**, 385–388 (2008).
28. Q. Guo *et al*., *Surf. Sci.* **604**, 1820–1824 (2010).
29. R. Ishikawa *et al*., *Nat. Mater.* **10**, 278–281 (2011).
30. J. Kliewer *et al*., *Science* **288**, 1399–1402 (2000).

ACKNOWLEDGMENTS

This work was performed, in part, at the Center for Nanoscale Materials, a U.S. Department of Energy Office of Science User Facility under Contract No. DE-AC02-06CH11357. This work was also performed, in part, at the NUANCE Center, supported by the International Institute for Nanotechnology, Materials Research Science and Engineering Centers (NSF DMR-1121262), the Keck Foundation, the State of Illinois, and Northwestern University. A.J.M., B.K., J.D.W., X.L., J.R.G, M.C.H., and N.P.G acknowledge support by the U.S. Department of Energy SISGR (contract no. DE-FG02-09ER16109), the Office of Naval Research (grant no. N00014-14-1-0669), and the National Science Foundation Graduate Fellowship Program (DGE-1324585 and DGE-0824162). X.-F.Z thanks the National Science Foundation of China (grant no. 11174152), the National 973 Program of China (grant no. 2012CB921900), and the Program for New Century Excellent Talents in University (grant no. NCET-12-0278). U.S. thanks the National Council of Science and Technology, CONACyT (proposal no. 250836). A.R.O acknowledges support fromthe Defense Advanced Research Projects Agency (grant no. W31P4Q1210008) and the Government of Russian Federation (no. 14.A12.31.0003). D.A., M.J.Y, and A.P. acknowledge support by the National Institute on Minority Health and Health Disparities (NIMHD) in the program Research Centers in Minority Institutions Program (RCMI) Nanotechnology and Human Health Core (grant G12MD007591), the NSF PREM DMR (grant no. DMR-0934218), the Welch Foundation (grant no. AX-1615), and the Department of Defense (grant no. 64756-RT-REP).

SUPPLEMENTARY MATERIALS

www.sciencemag.org/content/350/6267/1513/suppl/DC1
Materials and Methods
Supplementary Text
Figs. S1 to S13
References (*31*–*57*)

27 July 2015; accepted 28 October 2015
10.1126/science.aad1080

BATTERIES

Visualization of O-O peroxo-like dimers in high-capacity layered oxides for Li-ion batteries

Eric McCalla,[1,2,3,4] Artem M. Abakumov,[5,6] Matthieu Saubanère,[2,3,7] Dominique Foix,[2,3,8] Erik J. Berg,[9] Gwenaelle Rousse,[1,3,10] Marie-Liesse Doublet,[2,3,7] Danielle Gonbeau,[2,3,8] Petr Novák,[9] Gustaaf Van Tendeloo,[5] Robert Dominko,[4] Jean-Marie Tarascon[1,2,3,10]*

Lithium-ion (Li-ion) batteries that rely on cationic redox reactions are the primary energy source for portable electronics. One pathway toward greater energy density is through the use of Li-rich layered oxides. The capacity of this class of materials (>270 milliampere hours per gram) has been shown to be nested in anionic redox reactions, which are thought to form peroxo-like species. However, the oxygen-oxygen (O-O) bonding pattern has not been observed in previous studies, nor has there been a satisfactory explanation for the irreversible changes that occur during first delithiation. By using Li_2IrO_3 as a model compound, we visualize the O-O dimers via transmission electron microscopy and neutron diffraction. Our findings establish the fundamental relation between the anionic redox process and the evolution of the O-O bonding in layered oxides.

Because lithium-ion (Li-ion) batteries have the highest energy density of all commercially available batteries, they are able to power most consumer electronics and have emerged as the technology of choice for powering electric vehicles. Li-ion batteries may also be used for grid storage and load-leveling for renewable energy. Current state-of-the-art positive electrodes use layered rock salt oxides ($LiCoO_2$ and its derivatives), spinel ($LiMn_2O_4$), or polyanionic compounds such as olivine-type $LiFePO_4$ (*1*). One push to increase the practical capacity limit of $LiCoO_2$ is via chemical substitution aimed at stabilizing the layered framework. The partial replacement of Co^{3+} with Ni^{2+} and Mn^{4+} has led to the $Li(Ni_xMn_yCo_{1-x-y})O_2$ layered oxides being coined as stoichiometric nickel manganese cobalt (NMC) oxides. These compounds have improved safety and capacities approaching 200 mA·hour/g. Further substitution of the transition metals by Li results in capacities exceeding 270 mA·hour/g. These materials are referred to as Li-rich layered